Bottom-Up SiO₂ Embedded Carbon Nanotube Electrodes with Superior Performance for Integration in Implantable Neural Microsystems
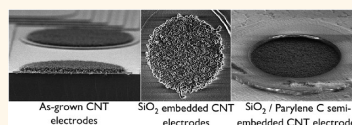
Silke Musa,[†,‡,*] Danielle R. Rand,[†] Daire J. Cott,[†] Josine Loo,[†] Carmen Bartic,[†,‡] Wolfgang Eberle,[†] Bart Nuttin,[§] and Gustaaf Borghs[†,‡]

[†]Imec, Kapeldreef 75, 3001 Heverlee, Belgium and [‡]Department of Physics and Astronomy and [§]Department of Neuroscience, KU Leuven, Oude Markt 13, 3000 Leuven, Belgium

Electrical recording and stimulation of the central nervous system is used in basic neuroscience to study brain functions[1,2] and in clinical practice to treat conditions such as epilepsy, Parkinson's disease, and chronic pain.[3] Device engineers are increasingly confronted with demands from neuroscientists and clinicians alike to develop implantable microsystems that provide high-density stimulation and recording capabilities integrated in one platform. These requirements are driven by the need to better understand the normal and abnormal dynamics of neural networks and provide spatially confined stimuli in order to alter disease states or induce behavioral, mnemonic, or cognitive changes. Ultimately, dense arrays with micrometer-sized electrodes for parallel and high-fidelity recording and selective stimulation of single neurons or neuronal populations are envisaged. Clearly, such strict device specifications can only be met by using advanced CMOS technology capable of addressing large electrode arrays in a reliable way.

Commonly used thin-film materials, including Pt, Ir, and TiN,[4] face serious limitations in terms of their potential for further electrode miniaturization. The electrode impedance, which scales inversely with the electrochemical interface capacitance and hence effective electrode area, may be too high—on the order of several MΩ—for small electrodes based on thin-film materials to provide sufficient recording sensitivity. In addition, the high driving voltages required to supply sufficient stimulation charge with small electrodes may damage the electrode and surrounding tissue. Solutions to mitigate these limitations aim at increasing the effective surface area (and

hence capacitance) of the electrodes by coating them with rough or porous materials, such as Pt black,[5] iridium oxide (IrOₓ),[6] conducting polymers,[7] and recently also carbon nanotubes (CNTs).[8-10] Platinum black suffers from poor mechanical stability, while IrOₓ and conducting polymers, such as poly-(3,4-ethylenedioxythiophene) and polypyrrole,

ABSTRACT

As-grown CNT electrodes | SiO₂ embedded CNT electrodes | SiO₂ / Parylene C semi-embedded CNT electrodes

The reliable integration of carbon nanotube (CNT) electrodes in future neural probes requires a proper embedding of the CNTs to prevent damage and toxic contamination during fabrication and also to preserve their mechanical integrity during implantation. Here we describe a novel bottom-up embedding approach where the CNT microelectrodes are encased in SiO₂ and Parylene C with lithographically defined electrode openings. Vertically aligned CNTs are grown on microelectrode arrays using low-temperature plasma-enhanced chemical vapor deposition compatible with wafer-scale CMOS processing. Electrodes with 5, 10, and 25 μm diameter are realized. The CNT electrodes are characterized by electrochemical impedance spectroscopy and cyclic voltammetry and compared against cofabricated Pt and TiN electrodes. The superior performance of the CNTs in terms of impedance ($\leq 4.8 \pm 0.3$ kΩ at 1 kHz) and charge-storage capacity ($\geq 513.9 \pm 61.6$ mC/cm^2) is attributed to an increased wettability caused by the removal of the SiO₂ embedding in buffered hydrofluoric acid. Infrared spectroscopy reveals an unaltered chemical fingerprint of the CNTs after fabrication. Impedance monitoring during biphasic current pulsing with increasing amplitudes provides clear evidence of the onset of gas evolution at CNT electrodes. Stimulation is accordingly considered safe for charge densities ≤ 40.7 mC/cm^2. In addition, prolonged stimulation with 5000 biphasic current pulses at 8.1, 40.7, and 81.5 mC/cm^2 increases the CNT electrode impedance at 1 kHz only by 5.5, 1.2, and 12.1%, respectively. Finally, insertion of CNT electrodes with and without embedding into rat brains demonstrates that embedded CNTs are mechanically more stable than non-embedded CNTs.

KEYWORDS: CNT electrodes · bottom-up SiO₂ embedding · neural probes · electrode impedance · charge injection · brain insertion

can degrade under electrical stimulation, leading to impedance fluctuations and loss of charge injection capacity.[11,12] In contrast, the long-term electrode viability is expected to improve significantly by using CNTs, which are chemically inert and stable against degradation under prolonged potential cycling.[13] Furthermore, CNTs exhibit excellent electrical conductivity and, most importantly, biocompatibility toward neurons.[14−18]

Recent studies have demonstrated CNT-coated electrodes with superior electrochemical performance compared to uncoated ones. These reports describe various methods to deposit the CNTs: chemical vapor deposition (CVD),[8,19−24] drop-coating,[25] pyrolysis of acetylene,[26] and microcontact printing.[27] Among these, only CVD can readily and reliably be applied at wafer-scale. However, conventional thermal CVD of CNTs requires temperatures far in excess (≫450 °C) of CMOS-compatible processing. Driven by the need to replace standard Cu-based interconnect technology, wafer-scale CVD synthesis of vertically aligned CNTs has been optimized to satisfy the temperature constraints of back-end-of-line (BEOL) CMOS processing and provide high-density, low-resistance CNT films.[28] While low-temperature CVD at 400 °C has been employed to grow CNTs on microelectrode arrays for ECoG recordings in rats,[29] this study failed to address the nontrivial aspect of mechanical stability of the CNT electrodes during the *in vivo* experiments. To our knowledge, no study has so far attempted to tackle the technological challenges and implications of integrating CNTs onto neural probes in a comprehensive and reliable way.

A key challenge here is ensuring the mechanical integrity of the CNTs during implantation.[30] The vertical structure of CVD-grown CNTs makes them susceptible to lateral abrasive forces during implantation, possibly leading to collapsed CNTs or even loss of material.[31] The former may cause electric shorts between neighboring electrodes especially on dense arrays. Appropriate embedding and lateral confinement of the CNTs may help overcome this problem. Technologically, two approaches may be sought: top-down or bottom-up embedding (Figure 1). With the former, CNTs are selectively grown in electrode openings defined in a top dielectric. This approach has the advantage that the CNT growth can be the last fabrication step, which may be beneficial to preserve the as-grown CNT properties. A challenge, however, is to match the height of the CNTs with the thickness of the dielectric in order to obtain an efficient embedding. Another drawback is that the catalytic metal film required for CNT growth by CVD cannot reliably and selectively be deposited within electrode openings of small dimensions. Consequently, the wafer surface will in part or wholly be coated with the potentially toxic metal catalyst and eventually a thin sheet of amorphous carbon. While *in vitro* neuronal survival of a few
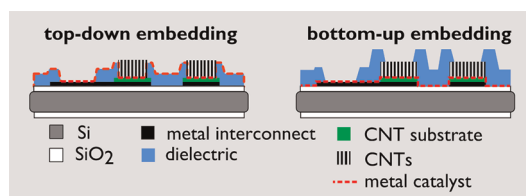

Figure 1. Comparison of top-down and bottom-up embedding of CNT electrodes.

days has been shown on such structures,[19,32] it is unclear whether catalytic metal traces will leach into the physiological medium or tissue during prolonged immersion.

For bottom-up embedding, which has been adopted in this work, a dielectric is deposited after CNT growth, and electrode openings are defined lithographically or possibly also by chemo-mechanical polishing.[33,34] In this approach, the metal catalyst present on the wafer surface is effectively covered (Figure 1). The major challenges are avoiding any damage and chemical modifications of the CNTs during the electrode opening and maintaining the biocompatibility of the CNTs throughout the fabrication process. For the latter, exposure of the CNTs to potentially toxic compounds, including organic substances such as photoresists and solvents, and metal contaminants must be prevented as they may become entrapped within the CNT matrix.[35,36] Thus, there were two main objectives in this study. First, we developed a robust fabrication process that allowed the wafer-scale integration of CNT microelectrodes for next generation neural probes with both recording and stimulation capabilities. Second, we demonstrated that the fabrication process did not compromise the electrodes' superior electrochemical performance and stability, chemical stability, and mechanical durability during insertion in the brain.

RESULTS AND DISCUSSION

Microelectrode arrays were fabricated on 200 mm Si wafers according to the scheme depicted in Figure 2. Briefly, for all investigated electrode materials, interconnects were defined by lift-off of sputter-deposited Pt (Figure 2a). Electrode arrays based on TiN and CNTs had an additional TiN layer on top of the electrode areas patterned by means of a second lift-off step (Figure 2b). Following reported procedures,[28] vertically aligned CNTs were selectively grown on the electrodes by a low-temperature (425 °C) plasma-enhanced CVD (PECVD) process using a 2 nm (nominal) thick Ni layer as a catalyst (Figure 2c and Figure 3a). The resulting multiwalled CNTs had a homogeneous height of ≈2 μm, an average diameter of 34 nm (determined by scanning electron microscopy (SEM)), and a density of approximately 2×10^{11} cm^{-2} (Figure 3b). We opted for this CNT height in order to avoid too high topographies
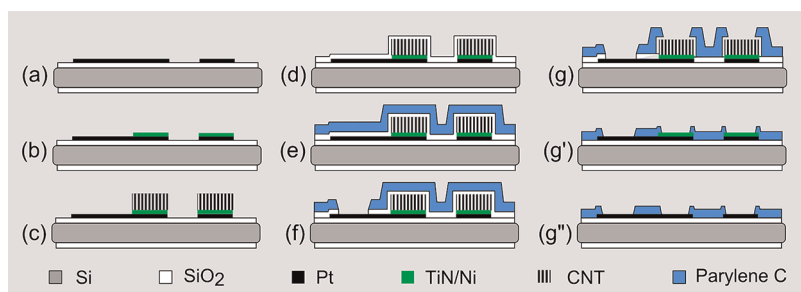
Figure 2. Schematic of the process flow for the (g) CNT, (g′) TiN, and (g″) Pt electrode arrays. For the fabrication of the Pt electrodes, steps (b–d) were omitted. For the fabrication of the TiN electrodes, steps (c,d) were omitted.
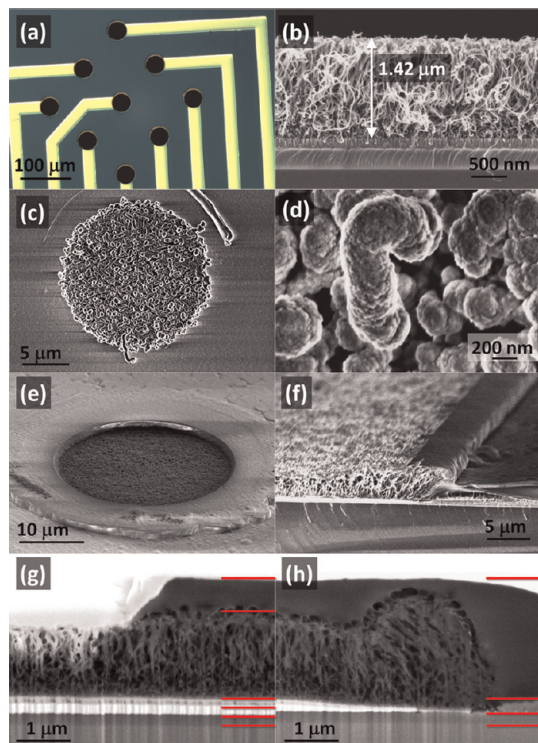

Figure 3. (a) Optical micrograph of an electrode array after CNT growth on top of the electrodes. (b) Cross-sectional SEM image of the as-grown CNTs. (c) SEM image of an electrode. (d) Zoom of (c) after conformal CVD SiO_2 coating. (e) Overview SEM image of an electrode after etching of the Parylene C and removal of the CVD SiO_2 in buffered HF. (f) Overview SEM image of a typical electrode edge partially encased in Parylene C. (g) Combined FIB/SEM image showing details of the final CNT−Parylene C interface at an electrode opening. The layers indicated with red lines are (from top to bottom) Parylene C, CNTs, TiN, Pt, thermal SiO_2. (h) Combined FIB/SEM image showing details of the final CNT−Parylene C interface at the outermost electrode edge. The indicated layers are (from top to bottom) Parylene C, CVD SiO_2, thermal SiO_2.

on the wafer surface and hence ensure a reliable lithography. The CNTs were embedded in 300 nm SiO_2 to serve as a protection and etch stop layer during subsequent fabrication steps. The SiO_2 was deposited by CVD at 150 °C (Figure 2d) and formed a conformal coating on top of the CNTs as seen from the SEM images in Figure 3c,d. As a biocompatible and hermetic insulation material, 1 μm of Parylene C was evaporated

(Figure 2e). The bond pads were opened by reactive ion etching (RIE) of the Parylene C and SiO_2 (Figure 2f). In a second RIE step, the Parylene C on the electrode areas was opened. The etch time was adjusted to stop on top of the oxide layer and thus prevent damage to the embedded CNTs. The corresponding stack profiles for the TiN and Pt electrodes are shown in g′ and g″ of Figure 2, respectively.

The wafers were then diced, and the chips were wire-bonded onto custom-printed circuit boards. Prior to experimentation, the SiO_2 layer on top of the CNT electrodes was removed by dipping the packaged chips in buffered hydrofluoric acid (BHF) (Figure 2g). The SEM image in Figure 3e displays an electrode after RIE of Parylene C and removal of the SiO_2 in BHF. Due to this wet treatment and subsequent drying of the chips, capillary action caused a clustering of the CNTs, resulting in the formation of dense microbundles. A typical electrode edge partly encased in Parylene C is shown in the overview SEM image in Figure 3f.

Focused ion beam (FIB) combined with SEM was employed to analyze the details of the CNT−Parylene C interface at an electrode edge. A cross-sectional FIB/SEM image of the final electrode edge shows the CNT−Parylene C interface at the electrode opening (Figure 3g). Red lines indicate the different layers, which are (from top to bottom) Parylene C, CNTs, TiN, Pt, and thermal SiO_2. Also clearly visible are larger voids underneath the Parylene C stemming from the removal of the CVD SiO_2 by BHF. These voids are also discernible in the cross-sectional FIB/SEM image in Figure 3g, which displays the CNT−Parylene C interface at the outermost electrode edge. Here, the indicated layers are (from top to bottom) Parylene C, CVD SiO_2, and thermal SiO_2. Clearly, the BHF etch time was sufficient to remove the CVD SiO_2 on top of the CNTs and preserve the SiO_2 stack outside the perimeter of the electrode. This aspect is essential for maintaining an optimal insulation of the metal interconnects. From the FIB/SEM analysis, it also becomes evident that the embedding and subsequent electrode opening did not lead to evident morphological changes of the CNT forest. In principle, bottom-up embedding of the CNT electrodes could also be achieved by omitting

the Parylene C and using only a thick CVD SiO_2 layer. Such neural probes would, however, only be suitable for acute or short-term implantations due to the gradual deterioration of the SiO_2 insulation in contact with the saline environment.[37] For chronic implantations, a more robust coating, such as Parylene C, is necessary.[38]

All electrode materials were characterized electrochemically by cyclic voltammetry (CV) and electrochemical impedance spectroscopy (EIS) in phosphate buffered saline (PBS). Cyclic voltammetry is generally used to identify the nature and extent of faradaic and nonfaradaic electrode processes and determine the material-specific voltage limits for hydrogen and oxygen evolution, also termed the *water window*. During neural stimulation, it is advised to avoid the occurrence of faradaic reactions in general and gas evolution in particular because they may damage the electrode and/or release chemical species which may alter the tissue beyond physiologically tolerable levels.[39−43] The water window is generally regarded as the safe operational voltage range for stimulation. This assumption ignores, however, that the electrode (over)voltages determined by CV may depend on the sweep rate and hence the kinetic and diffusional dynamics of the underlying faradaic electrode processes.[44,45] Considering that the differential voltage "sweep rate" observed during stimulation can be more than 4 orders of magnitude larger than the slow sweep rate generally employed for CV, it is not plausible why voltage limits obtained by CV should correspond to the maximum electrode polarization tolerable under stimulation. This 1:1 translation should be assessed more critically to establish proper criteria for safe stimulation ranges.[46] The values for the water window determined in this work served solely to calculate the charge-storage capacity (CSC), which corresponds to the area under the CV curve divided by the voltage sweep rate. Mostly, only the cathodic branch of the CV curve is taken into consideration. This cathodic CSC (CSC_c) is a useful figure of merit to allow first-order comparisons of the charge-storage capability of various electrode materials under well-defined experimental conditions. Materials with a high CSC_c are also considered more efficient for stimulation.

Figure 4 shows typical voltammograms obtained with Pt, TiN, and CNT electrodes of 5 μm diameter. The Pt voltammogram exhibits the typical features of H adsorption and desorption between −0.6 and −0.3 V and a broad Pt oxidation band between 0.25 and 0.9 V. The large current step in the cathodic sweep between 0 and 0.2 V is due to the reduction of dissolved O_2. The sharp current increases at the end of the cathodic and anodic scans are due to the onset of H_2 and O_2 gas evolution, respectively. Electrodes based on TiN show a strong blocking behavior in the potential region −0.5−1.1 V where current flow is mostly capacitive in nature. In the anodic scan, two large bands centered

around −0.85 and −0.4 V can be observed and are attributed to the oxidation of H_2 gas and chemisorbed H, respectively.[47] Due to the lack of distinct H adsorption features in the cathodic scan, the onset potential for H_2 evolution cannot be identified. Thus, this is set at −0.75 V for the TiN electrodes. Further, in the anodic scan, an oxidative wave near 1.2 V was attributed to the formation of a surface oxynitride and/or oxide phase.[48,49] The reductive shoulders visible at approximately 0 and −0.25 V are considered to correspond to the reduction of this oxynitride and/or oxide layer. The signal at 1.1 V in the cathodic sweep may be related to the reduction of O_2 that evolved in the preceding anodic scan. Electrodes coated with CNTs show a strong capacitive response as evidenced by the large area under the CV curve and the lack of large faradaic features. Besides a well-defined reductive peak at −0.25 V and a weaker shoulder at −0.6 V, only ill-defined broad oxidation bands can be discerned. The overall redox activity of the CNT electrodes, including the reductive peak at −0.25 V, bears a strong resemblance to the voltammetric response of the bare TiN electrodes. This may indicate that the CNTs do not form a fully closed layer above the TiN substrate and that the electrolyte is able to enter the CNT matrix and spread over the TiN. This result is of great importance since it implies a good wettability of the CNT matrix. On the other hand, similar voltammetric features have also been reported for single-walled CNT sheets and were attributed to oxygen-containing functional groups present in the CNT sidewalls.[50] Thus, it remains unclear whether the observed redox activity is solely due to the TiN underlayer or is also caused by the CNTs. Only a small fraction of the overall charge available with CNTs is faradaic in nature, while most of the charge arises from the charging and discharging of the electrochemical double layer. Given this rather inert nature of the CNTs, fewer chemical modifications and hence degradation of the electrodes are expected during prolonged stimulation.

Visual comparison of the CV curves reveals that the CSC_c of the CNT electrodes is much larger than that of the Pt and TiN electrodes. Table 1 summarizes the CSC_c values (mean ± standard deviation) for all investigated electrode sizes and materials obtained from n_e different electrodes. Also provided are the CSC_c values normalized by the respective value of the 25 μm diameter electrode, CSC_c^{25}, and the voltage ranges of the water window. The CSC_c obtained with the CNT electrodes is more than 2 orders of magnitude larger than that of the Pt and TiN electrodes of the same diameter. It also appears that more charge per unit area is available with decreasing electrode diameter as indicated by the CSC_c^{25}. This behavior can be explained by the potentiodynamic current response of ultramicroelectrodes.[51] Here, the steady-state diffusion-limited current density, i_l, scales inversely with the
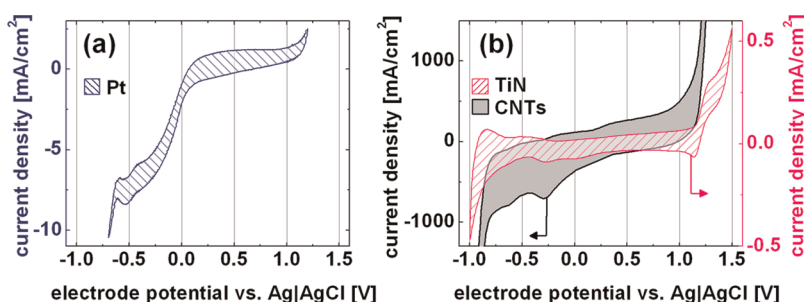
Figure 4. Cyclic voltammograms of (a) Pt, (b) TiN and CNT electrodes of 5 μm diameter each. Scans were performed at 0.1 V/s in phosphate buffered saline.

TABLE 1. Values for the CSC$_c$, CSC$_c^{25}$, and Water Window of Pt, TiN, and CNT Electrodes

material	Ø (μm)	CSC$_c$ (mC cm^{-2})	CSC$_c^{25}$ (au)	n_e	water window vs Ag|AgCl [V]
Pt	25	1.6 ± 0.2	1.0 ± 0.2	6	
	10	3.5 ± 1.6	2.2 ± 1.3	6	−0.60 to 0.90
	5	13.5 ± 3.0	8.6 ± 2.9	8	
TiN	25	3.0 ± 1.3	1.0 ± 0.7	8	
	10	5.4 ± 1.1	1.8 ± 1.4	5	−0.75 to 1.10
	5	19.8 ± 1.7	6.7 ± 2.8	6	
CNTs	25	513.9 ± 61.6	1.0 ± 0.2	12	
	10	2012.0 ± 208.2	3.9 ± 0.9	13	−0.75 to 1.10
	5	6612.1 ± 394.5	12.9 ± 2.3	12	

electrode radius:

$$i_l = \frac{4nDC^*}{\pi r_e} \tag{1}$$

where n is the number of electrons, D is the diffusion coefficient, C^* is the bulk analyte concentration, and r_e is the electrode radius. Hence, for electrodes with 5 and 10 μm diameter, the current density is expected to increase by a factor of 5 and 2.5, respectively, compared to a 25 μm diameter electrode. This is in good agreement with the range of CSC$_c^{25}$ values in Table 1 except for the 5 μm diameter CNT electrodes, which accommodate a larger charge density than expected. This is most likely caused by slight lithography-related differences between the actual and nominal geometric electrode area. Although not unexpected, the increase in CSC$_c$ with decreasing electrode area is an interesting aspect for neural stimulation with small electrodes and requires further investigation under realistic stimulation conditions.

The water window for Pt (Table 1) was smaller than for the other materials, which can be attributed to the electrocatalytic nature of Pt toward hydrogen and oxygen evolution. Slightly different water windows have also been reported for Pt and TiN electrodes.[4] However, as mentioned earlier, values for the water window determined by CV should not be regarded as operational limits for electrodes under stimulation. They serve solely to determine the CSC$_c$ and hence the capability of a material to store charge at a given sweep rate. From the CSC$_c$, it becomes clear that the

CNTs are by far the most effective (at the given sweep rate).

Electrochemical impedance spectra were recorded for all electrode sizes and materials at their respective equilibrium potentials. The EIS data were analyzed by the fitting to physically meaningful equivalent circuit models and by parameter extraction. The linear frequency response of an electrode−electrolyte interface can be modeled in terms of an equivalent circuit where the individual circuit elements describe the various relaxation phenomena occurring at the interface. In a first approach, the interface behaves like a parallel RC circuit, where the resistance represents the faradaic response of the system, termed the charge-transfer resistance, R_{ct}, and the capacitance provides information on the interfacial charge distribution known as the double layer capacitance, C_{dl}. The C_{dl} is largely responsible for the neural signal transduction across the electrode−tissue interface and should be designed to be as large as possible in order to detect the minute neuronal signals. In general, more complex circuit models need to be employed to account for diffusion phenomena, chemical modifications at the electrode surface, and distributed relaxation phenomena arising with electrode materials that exhibit a certain porosity or surface roughness.[52] In this last case, the capacitive nature of the interface is represented by a constant-phase element (CPE), which is characterized by a frequency-independent phase angle. Its impedance, Z_{CPE}, shows an empirically determined power law frequency dependence:

$$Z_{CPE} = \frac{1}{A_{CPE}(i\omega)^\alpha} \tag{2}$$

where ω is the angular frequency, A_{CPE} is a measure of the magnitude of Z_{CPE}, and $0 < \alpha < 1$ is a measure for the system's deviation from an ideal capacitive response for which $\alpha = 1$. In general, α is considered to depend on the roughness of an electrode material and decreases with increasing roughness.

The efficiency of a recording electrode is measured in terms of its impedance magnitude at 1 kHz, which is the characteristic frequency in the power spectrum of a neural action potential with a duration of 1 ms. Low

electrode impedances are generally associated with low intrinsic noise levels leading to high signal-to-noise ratios. Besides the noise level, the impedance as a function of the geometric electrode area also affects the recorded signal amplitude, that is, the recording sensitivity.[53] The recording sensitivity decreases with increasing electrode area because of spatial averaging of the voltage across the (geometric) electrode area. Thus, while small electrodes with a relatively high impedance may have a larger intrinsic noise, their signal-to-noise ratio may still be higher than that of large electrodes with a lower impedance due to a higher recording sensitivity.[54] Recent studies furthermore suggest that low-impedance coatings such as CNTs can also lead to a significant improvement in recording sensitivity compared to uncoated electrodes of similar size.[9,55,56] The observed effects are, however, not yet understood.

Figure 5 shows the Bode plots of all electrode sizes and materials averaged over n_e measurements from n_e different electrodes (see Table 2 for the values of n_e). Figure 6a shows the impedance magnitudes at 1 kHz of the measured electrode materials and the theoretical behavior of a flat microelectrode in function of the electrode diameter. The theoretical impedance magnitude was determined according to

$$|Z|(f) = \frac{1}{2\pi f \times A \times 20 \,\mu F/cm^2} \tag{3}$$

where $f = 1$ kHz is the frequency and $20 \,\mu F/cm^2$ is the specific capacitance of a flat electrode.[57] For all electrode sizes, the CNT electrode impedance is 3 orders of magnitude lower compared to the Pt and TiN electrodes. In contrast, impedances of previously reported CNT electrodes of similar dimensions are 10 times higher ($60-100$ kΩ[23]). There are likely to be several reasons for this difference possibly related to the CNT density and structure, the chemical properties of the CNTs, and the substrate, among others. Noteworthy is the strong deviation of the impedance magnitude for the 5 and 10 μm diameter Pt and TiN electrodes from the theoretical behavior. Such deviations cannot be caused by fabrication errors alone, which are at most $\pm 1 \,\mu$m for lithography and RIE together, but are most likely due to parasitic capacitances, which become more dominant with decreasing electrode size. Furthermore, both the impedance and CSC_c of the CNT electrodes remained unchanged after storage in a nitrogen drybox for more than 1 year postprocessing. This aspect is essential in terms of longterm electrode reliability.

For all Pt electrode sizes in Figure 5, the phase angle, θ, remains close to the value of an ideal capacitor for which $\theta = -90°$. In contrast, the TiN electrodes exhibit a clear minimum of $|\theta|$ between 10^2 and 10^3 Hz, which implies a slightly stronger faradaic contribution than with Pt. Electrodes coated with CNTs behave
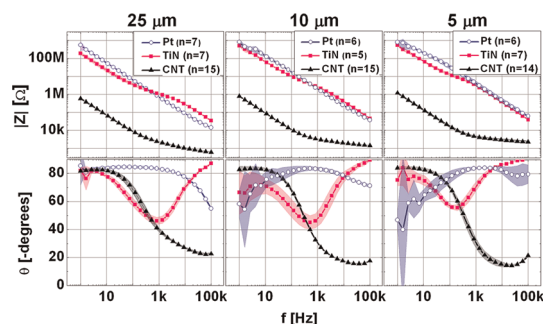

Figure 5. Average Bode plots (mean $\pm$ standard deviation) with impedance magnitude, $|Z|$, and phase angle, θ, for the Pt, TiN, and CNT electrodes of 25, 10, and 5 μm diameter measured between 1 and 10^5 Hz in phosphate buffered saline.

capacitively at low frequencies and resistive at higher frequencies similar to an electronic high-pass filter. Least-square fitting of the spectra reveals that this effect originates from various relaxation processes involving chemical modifications at the CNT surface and a low R_{ct} combined with the occurrence of diffusion. The equivalent circuit is provided in Figure 6b. The series resistance, R_s, accounts for the ohmic behavior of the solution and metal wires. For the TiN and CNT electrodes, an additional capacitance, C_x, is included in series with R_{ct}. In the case of CNTs, it has been recognized that a small fraction of the interfacial capacitance is faradaic rather than electrostatic in nature and is termed the pseudocapacitance.[58] It is considered to originate from functional groups (defects) present at the tip and sidewalls of the CNTs, which are redox-active. In general, pseudocapacitances can arise due to chemisorption or redox reactions occurring at electrode surfaces. The charge that is transferred in these electrode processes is some function of the electrode potential and, as such, resembles the behavior of a capacitance. Importantly, this kind of capacitance is faradaic in nature, rather than being associated with a potential-dependent distribution of electrostatic charge as for the C_{dl}.

The pseudocapacitance is represented as a capacitance, C_x, in series with R_{ct}. In the case of TiN, C_x may be related to the presence of an insulating oxide and/or oxynitride layer on top of the electrodes introduced during the electrode opening by RIE.[34] In particular, for the CNT electrodes, an additional distributed element, the Warburg impedance, Z_W, was required to account for diffusion effects in the porous matrix. It is connected in series with R_{ct} and C_x. In general, diffusion occurs as a consequence of charge-transfer reactions taking place at an electrode and depleting the adjacent electrolyte from reactants. It is therefore directly related to the magnitude of R_{ct}, which is a measure of the kinetic feasibility of a faradaic reaction. If charge transfer is hindered due to sluggish reaction kinetics and thus a large R_{ct}, diffusion will not become a

TABLE 2. Average Fitting Parameters (with Standard Deviations) for the Pt, TiN, and CNT Electrodes of 25, 10, and 5 μm Diameter

| material	Ø (μm)	R_s (kΩ)	R_{ct} (kΩ)	A_{CPE} (nF s$^{\alpha-1}$)	α	A_W (mF s$^{-0.5}$)	C_x (pF)	C_i (pF)	n_e
Pt	25	20.38 ± 2.65	(6.23 ± 0.31) × 10^6	0.32 ± 0.05	0.92 ± 0.00	n/a	n/a	56.46 ± 4.33	7
	10	80.81 ± 17.97	(1.36 ± 1.09) × 10^6	0.13 ± 0.05	0.89 ± 0.03	n/a	n/a	32.21 ± 2.82	6
	5	(4.69 ± 2.70) × 10^2	(2.12 ± 1.58) × 10^5	0.05 ± 0.02	0.89 ± 0.04	(5.70 ± 2.49) × 10^{-4}	n/a	23.93 ± 1.43	7
TiN	25	(0.83 ± 0.10) × 10^3	(0.53 ± 0.15) × 10^4	0.86 ± 0.18	0.84 ± 0.02	n/a	(2.49 ± 0.74) × 10^2	49.38 ± 2.51	7
	10	(2.56 ± 1.51) × 10^3	(1.78 ± 0.82) × 10^4	0.39 ± 0.14	0.78 ± 0.06	n/a	75.83 ± 25.38	38.79 ± 4.52	5
	5	(7.02 ± 0.97) × 10^3	(2.31 ± 0.79) × 10^4	0.30 ± 0.08	0.80 ± 0.06	n/a	67.74 ± 8.53	43.19 ± 2.78	7
CNTs	25	0.63 ± 0.05	1.23 ± 0.14	(1.39 ± 0.32) × 10^2	0.83 ± 0.02	11.73 ± 1.49	(1.92 ± 0.35) × 10^5	(6.72 ± 0.53) × 10^2	16
	10	1.15 ± 0.33	1.47 ± 0.13	(0.81 ± 0.24) × 10^2	0.85 ± 0.03	11.43 ± 2.25	(1.52 ± 0.20) × 10^5	(4.24 ± 2.33) × 10^2	15
	5	2.37 ± 0.33	1.51 ± 0.21	(0.65 ± 0.12) × 10^2	0.86 ± 0.02	10.58 ± 2.47	(0.87 ± 0.13) × 10^5	(2.24 ± 0.31) × 10^2	14
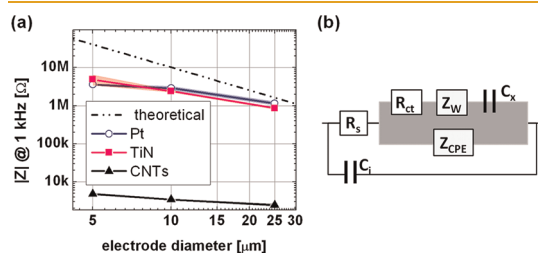
Figure 6. (a) Dependence of the electrode impedance magnitude at 1 kHz on the electrode radius: comparison of theoretical (flat disk electrode) and experimental data for the Pt, TiN, and CNT electrodes. The experimental values are averaged over n_e measurements from n_e different electrodes (see Table 2 for the n_e values). (b) Equivalent circuit used to fit the impedance spectra.

limiting factor. Its contribution to the observed impedance will hence be negligible. On the other hand, facile reaction kinetics, or equivalently a small R_{ct}, is accompanied by a fast depletion of reactants at the interface. The measured reaction rate becomes diffusion-limited and will be registered as an additional impedance. The Z_W is described by the same equation as Z_{CPE} (eq 2), but with a constant power factor, $\alpha = 0.5$. Parasitic capacitances due to the Parylene C insulation are described by the lumped capacitance, C_i.

Table 2 provides the fit parameters for all electrode sizes and materials. The R_s shows a strong dependence on the electrode material and is up to 3 orders of magnitude higher for the Pt and TiN electrodes as compared to the CNT electrodes. The R_s of the CNT electrodes is largely determined by the low solution resistance (the metal interconnect resistance can be neglected), which is a direct consequence of the large distributed surface area of the CNTs, and can be described in terms of a porous electrode:[52]

$$R_{s,p} = \frac{\rho l}{r_p^2 \pi n_p} \tag{4}$$

where ρ is the solution resistivity, l is the pore length, r_p is the pore radius, and n_p is the number of pores. For comparison, the solution resistance in the case of a recessed disk electrode with radius r_e and a recess height h is[59]

$$R_{s,e} = \frac{\rho}{4r_e} + \frac{\rho h}{r_e^2 \pi} \tag{5}$$

where $h = 1$ μm corresponds to the Parylene C thickness. The average diameter of a nanotube in this work is 34 nm. Assuming that the CNTs are arranged in a dense square lattice, the pores corresponding to the void space between the nanotubes can be approximated by cylinders with a radius $r_p = 7$ nm. Further, the total number of pores equals the number of nanotubes, that is, $n_p = 9.8 \times 10^5$ for the 25 μm diameter electrode, and the pore length corresponds to the height of the CNT film, $l \approx 2$ μm. Using these values and a PBS resistivity of $\rho = 70$ Ω cm, one obtains for a 25 μm diameter electrode $R_{s,p} = 9.3$ kΩ and $R_{s,e} = 15.4$ kΩ. The latter is in good agreement with the value for a Pt electrode in Table 2. In contrast, the actual R_s for the CNT electrodes is more than an order of magnitude lower than the theoretical $R_{s,p}$. Considering that the CNT length and density are reliably controlled during the growth process, the most uncertain factor in eq 4 is r_p. It can strongly be affected by the fabrication process and most likely covers a broad range of values. This also becomes evident from the SEM images in Figure 3b,f. The actual r_p for a 25 μm diameter electrode is therefore about 4 times larger than estimated. For the 10 and 5 μm diameter CNT electrodes, one obtains 7 and 10 times larger r_p values, respectively, than estimated. The bare TiN electrodes show an unexpected high R_s. This may be due to a higher intrinsic resistivity of the TiN layer possibly caused by oxidation during RIE of Parylene.

The R_{ct} for the Pt and TiN electrodes is 4—6 orders of magnitude higher than for the CNT electrodes. Thus, charge transfer occurs much easier at the CNTs than at

the Pt or TiN electrodes, which also explains why diffusional involvement in the form of the Z_W was mostly observed for the CNT electrodes. The extent to which this enhanced reactivity of the CNTs may or may not be beneficial for neural recording and stimulation remains to be determined.

The low impedance of the CNT electrodes is a direct consequence of their large interfacial capacitance. This is reflected by A_{CPE} values in Table 2, which are 2–3 orders of magnitude higher than for the Pt and TiN electrodes. The CPE power factor, α, of the Pt electrodes is close to unity and thus resembles the behavior of an ideal capacitor. The TiN and CNT electrodes have a smaller α, which indicates a higher roughness/porosity. The roughness of TiN is caused by its microcolumnar morphology.

The CNT pseudocapacitance, C_x, is of the same order of magnitude as A_{CPE} and therefore directly related to the large specific surface area of the CNTs. Although faradaic and not electrostatic in nature like the CPE, a large C_x may similarly improve the quality of the signal transduction across the electrode–tissue interface and enhance charge injection during stimulation. On the other hand, the influence of Z_W on the performance of neural electrodes is not evident. Finally, C_i is 1 order of magnitude higher for the CNT electrodes. Here, additional parasitic coupling compared to the planar Pt and TiN electrodes may occur through the Parylene C encasement of the vertical electrodes (see Figure 2g and Figure 3f).

In the experiments described so far, we demonstrated that the large distributed interface capacitance endows the CNT electrodes with a superior capability to store charge and consequently also with a very low impedance. While allowing first-order qualitative judgements about electrode performance, the voltammetric analysis does not represent a realistic stimulation scenario. Here, fast biphasic rectangular current pulses are applied that give rise to nonlinear potential changes on the order of kV/s. Under these charging conditions, interfacial processes may be governed by different kinetic and diffusional dynamics than during slow-sweep voltammetry. Moreover, the transmission-line effect of the porous CNT matrix may limit the effective surface area contributing to capacitive charging and charge transfer at the interface.[60] Consequently, only a fraction of the expected charge density may be accessible at the fast charging rates occurring under stimulation.

In order to investigate the safe operational limits of electrical stimulation with CNT electrodes, that is, the charge density at which hydrolysis occurs, we applied biphasic, charge-balanced, cathodic-first, symmetric current pulses of 400 μs phase width and increasing amplitude and monitored the voltage transients. The maximum applied current amplitude was determined by the maximum voltage range of the potentiostat (± 10 V). For the 25 μm electrodes characterized here, amplitudes ranged from 100–2150 μA in increments of 50 μA corresponding to charge densities of

8.1–175.2 mC/cm^2. For each current amplitude, trains of 50 pulses were applied at 100 Hz, which is a typical frequency for neural stimulation.[61] Figure S-1 of the Supporting Information shows the voltage transients of the 50th pulse for each applied amplitude. After every fifth increase in pulse amplitude (i.e., after every 250 pulses), an impedance spectrum was recorded (Figure S-2a of the Supporting Information). The relative change in impedance magnitude with respect to the prestimulation values, $|Z|_0$, is shown in Figure 7a for the exemplary frequencies of 10 Hz, 1 kHz, and 100 kHz.

The relative impedance changes remained almost constant up to 60 mC/cm^2 and then started to gradually increase. This increase was most evident for the 100 kHz trace. We further analyzed the impedance data by means of fitting to the equivalent circuit in Figure 6b and observed a similar charge density dependence for R_s (Figure 7b). The fit values of R_s were nearly identical to the measured values of $|Z|$ at 100 kHz, which was expected, considering that the impedance magnitude at very high frequencies is dominated by the electrode's series resistance. In Figure 7c, we furthermore plot the fit values for C_i. Surprisingly, here we observed a linear decrease in capacitance starting at 40.7 mC/cm^2.

Both phenomena, the increase in R_s (or $|Z|$(100 kHz)) and the decrease in C_i may be explained by the evolution of gas bubbles. A graphical representation of the possible mechanism is shown in Figure 8. Gas bubbles formed within the CNT matrix partially block the available current path, which in turn increases the ohmic voltage drop and hence R_s. On the other hand, small gas bubbles can accumulate under the Parylene C insulation and act as an additional small capacitance in series to C_i thus decreasing the effective shunt capacitance. With increasing charge density, more gas bubbles form leading to a gradual increase of R_s and a decrease of C_i. Thus, for our electrodes, the safe stimulation charge density was fixed at 40.7 mC/cm^2. This is only 7.9% of the voltammetric charge-storage capacity determined for 25 μm diameter CNT electrodes (cf. Table 1), but 2 orders of magnitude larger than the charge-injection limit of 0.5 mC/cm^2 determined for Pt microelectrodes in a previous study.[46]

Typical charge thresholds reported for evoking neural activity using microstimulation revolve around 9 nC.[62] Thus, on the basis of the above safe stimulation limits of Pt and CNT electrodes, the smallest electrodes that can safely supply sufficient charge to activate neural tissue are 47.9 and 5.3 μm in diameter, respectively, if we assume that the safe charge scales linearly with the electrode area. Thus, the relatively high safe stimulation charge density of the CNT electrodes offers the potential for further electrode miniaturization and for higher stimulation selectivity than achievable with standard thin-film materials such as Pt.

In order to determine the stability of the CNT electrodes during long-term stimulation, we applied
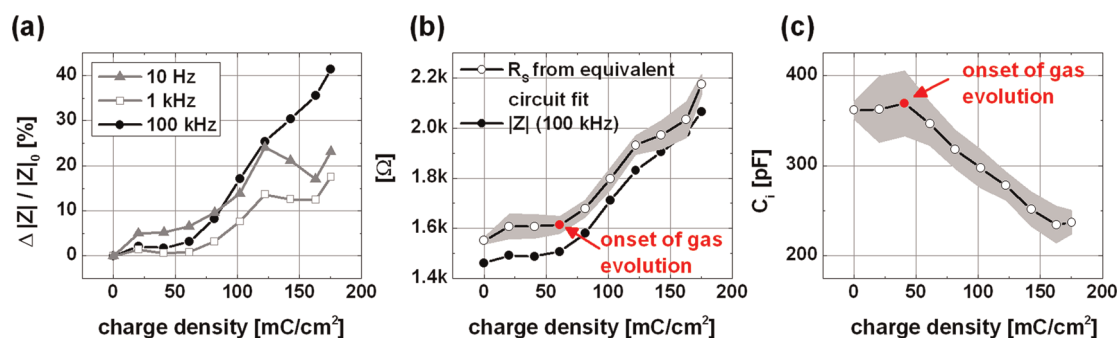
Figure 7. (a) Dependence of the relative impedance change, $\Delta|Z|/|Z|_0$, on the stimulation charge density for 10 Hz, 1 kHz, and 100 kHz. (b) Dependence of R_s obtained from fitting to the equivalent circuit in Figure 6b and $|Z|$(100 kHz) on the applied charge density. (c) Dependence of C_i on the applied charge density. Fit errors are shown as gray bands around R_s and C_i.
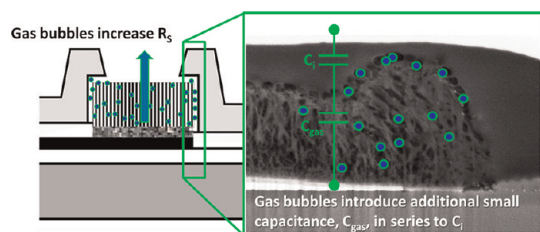

Figure 8. Graphical representation of the impact of gas bubble formation on the R_s (left panel) and C_i (right panel) of a CNT electrode.

Figure 9. Basline-corrected transmittance infrared spectra of (a) as-grown CNTs, (b) SiO$_2$-coated CNTs after BHF treatment, and (c) CNTs after BHF treatment. The corresponding contact angles for the three substrates are shown on the right-hand side.

trains of 50 biphasic, charge-balanced, cathodic-first, symmetric pulses of either 8.1, 40.7, or 81.5 mC/cm^2 up to a total of 5000 pulses and monitored the impedance every 250 pulses. The recorded voltage transients of the 50th and 5000th pulse for each charge density are shown in Figure S-4 of the Supporting Information. Only minor changes in voltage amplitude were observed with increasing number of pulses. The percent changes in impedance magnitude at 1 kHz with respect to the pre-stimulation values remained largely constant after the initial 1000 pulses reaching at most 5.5, 1.2, and 12.1% for 8.1, 40.7, and 81.5 mC/cm^2, respectively. Equivalent circuit analysis of the impedance spectra revealed no noteworthy changes except a slight increase of R_s and decrease of C_i for the highest stimulation charge density (see Figure S-9 of the Supporting Information). As already discussed above, this is most likely a consequence of the formation of gas bubbles in the CNT matrix. Overall, we can say that prolonged stimulation even above the gas evolution limit has only marginal impact on the performance of the CNT electrodes in terms of low impedance.

It is known that chemical modifications by acid treatment and/or exposure to oxygen plasma can profoundly change the properties of CNTs, including hydrophobicity and biocompatibility.[63,64] Avoiding chemical changes of the CNTs during device fabrication was an important aspect of process reliability in this work and would allow for specific and controlled modifications of CNT post-processing. In order to investigate the impact of the different processing steps on the chemical properties of the CNTs, we
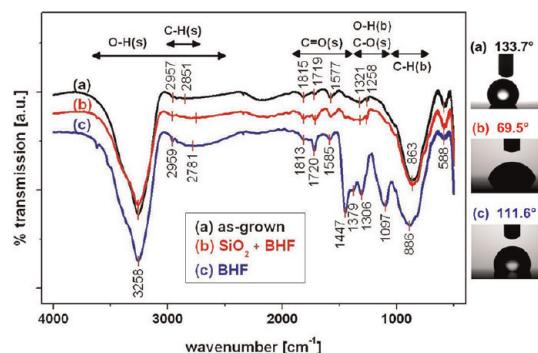
performed FTIR analysis and contact angle measurements. Figure 9 shows the baseline-corrected FTIR spectra and contact angles determined from as-grown CNTs, BHF-treated CNTs, and BHF-treated SiO$_2$-coated CNTs similar to the fabrication sequence of the real devices. The exposure to BHF was always 1.5 min. All spectra contain a broad band with a maximum near 3258 cm^{-1} originating from stretching modes related to various O−H containing surface groups.[65,66] A weak band centered around 2700 cm^{-1} may be caused by O−H and C−H stretching modes.[67] The signals at 1813, 1720, and 1585 cm^{-1} are assigned to C=O stretching modes.[67−69] In addition, for the BHF-treated sample, a strong peak appeared at 1447 cm^{-1}, which also describes C=O stretching vibrations.[68,69] Signals in the region 1400−1000 cm^{-1} are assigned to O−H bending and/or C−O stretching modes.[67,68] A strong peak in this region at 1097 cm^{-1} was observed for the BHF-treated sample. The band at approximately 850 cm^{-1} is attributed to C−H bending modes.[67] Clearly, the BHF treatment introduces additional O-containing functional groups. In contrast, the spectrum of the BHF-treated SiO$_2$-coated CNTs does not reveal any significant changes to the as-grown CNTs, which indicates that the BHF exposure time is sufficient to remove the oxide and leave the CNTs unaltered. The results also indicate that functional groups are to some
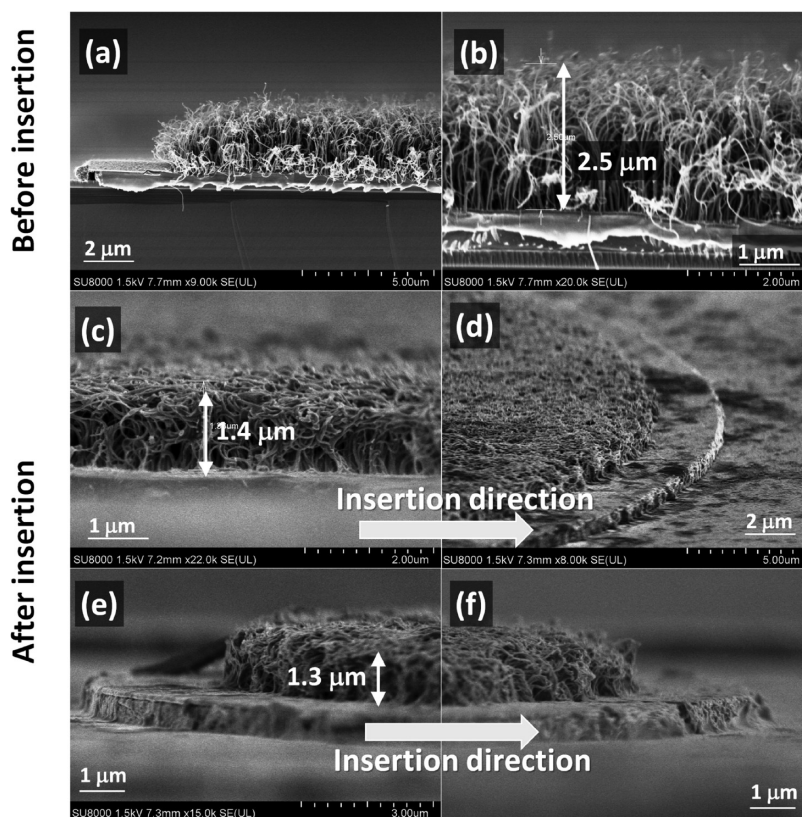
Figure 10. (a,b) SEM images of a non-embedded CNT electrode before insertion. (c—f) SEM images of non-embedded CNT electrodes after insertion. Indicated is the direction of insertion.
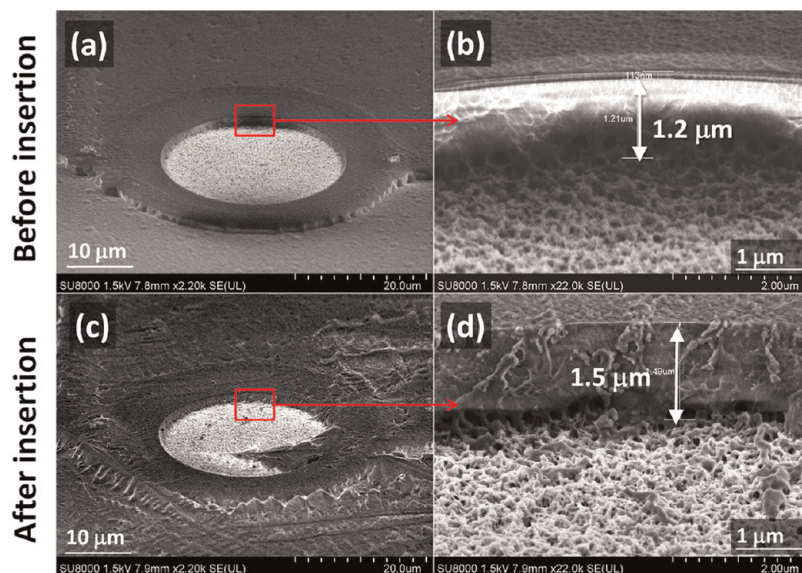

Figure 11. (a) SEM image of an embedded CNT electrode prior to insertion. (b) Zoom of the Parylene C edge at the electrode opening before insertion. (c) SEM image of the CNT electrode after insertion. (d) Zoom of the Parylene C edge after insertion.

extent present in the as-grown CNTs. The contact angle is lowest for the BHF-treated SiO_2-coated CNTs. The BHF treatment of the as-grown CNTs only marginally improved their wettability, which is unexpected considering the largest IR signal increase due to hydrophilic functional groups. Therefore, the improved wettability of the BHF-treated SiO_2-coated CNTs is

rather physical than chemical in nature. It was indeed shown that a better hydrophilicity can be achieved with CNT films that have an open microtexture as opposed to closed unmodified CNT films.[70] The appearance of microbundles on the BHF-treated SiO_2-coated CNTs may hence account for the reduced contact angle. On the other hand, no microbundles

were observed after BHF treatment of the as-grown CNTs. This demonstrates that the presence of the SiO$_2$ is essential for mediating the BHF into the CNT matrix and eventually forming the microbundles, which improve the wettability.

The mechanical stability of CNT electrodes fabricated with and without embedding was evaluated by inserting the chips in explanted rat brains (Figure S-8a, b of the Supporting Information) using a microdrive. Figure 10a—f shows SEM images of the non-embedded electrodes before and after insertion. Insertion led to a compression of the CNTs with their height decreasing by 1.2 μm from 2.5 to 1.3 μm. Similar behavior was also observed for uniformly grown (unpatterned) CNT films after insertion in the brain (Figure S-9 of the Supporting Information). These results also suggest that the adhesion of the CNTs to the substrate is sufficiently strong to prevent abrasion or material loss during insertion. For the embedded electrodes (Figure 11a—d), the CNT compression due to insertion was determined by measuring the height of the Parylene C at the electrode opening. This height changed only by 300 nm from 1.2 to 1.5 μm. Clearly, the embedded CNTs are less compressed after insertion. Whether this is a consequence of the shielding effect provided by the Parylene C or due to the CNT densification after SiO$_2$ removal, which prevents any further compression, is not apparent. Further implantations using densified CNT electrodes without Parylene C will clarify this. The implantation results show that bottom-up embedding is a good strategy for mechanically preserving CNT electrodes.

CONCLUSIONS

One of the major technological challenges toward using vertically aligned CNTs as an electrode material in implantable neural microsystems relates to the fabrication process. An appropriate process integration scheme must provide a reliable embedding to protect the CNTs during fabrication, handling, and implantation in the brain and at the same time not compromise their electrochemical performance. In this paper, we demonstrated for the first time the fabrication of CNT microelectrodes using a bottom-up embedding approach. All processing parameters were compatible with wafer-scale BEOL CMOS processing as required for realizing advanced neural probes with high-density and high-resolution electrode arrays. Low-temperature (425 °C) PECVD was employed to grow vertically aligned multiwalled CNTs on passive arrays comprising microelectrodes of 5, 10, and 25 μm diameter. Our process involved embedding CNT electrodes using a coating stack comprising SiO$_2$ and Parylene C with lithographically defined electrode openings. The SiO$_2$ acts as a chemical and mechanical protection of the CNTs during the fabrication process and during handling and is removed only after packaging of the devices. The use of BHF to remove the SiO$_2$ was shown to greatly improve the wettability of the CNTs while preserving their chemical fingerprint as determined by FTIR. The Parylene C insulation lessened the compression of the CNT electrodes experienced during implantation. In contrast, non-embedded CNT electrodes were strongly compressed during implantations and lost much of their initial form factor, which renders them less reliable. Another major advantage of our bottom-up process is that the potentially toxic metal catalyst used to grow the CNTs is effectively covered. *In vitro* experiments using dissociated neuron cultures are currently underway to prove that indeed neuronal viability is preserved on these substrates. The functionality and performance of the fabricated and packaged electrode arrays was assessed by CV and EIS in PBS and compared against cofabricated Pt and TiN microelectrodes. For all electrode diameters, the CNT electrode impedance at 1 kHz ($\leq$4.8 $\pm$ 0.3 kΩ) was 3 orders of magnitude smaller compared to the Pt and TiN electrodes. Also, the CNT electrodes outperformed the Pt and TiN electrodes in terms of the CSC$_c$ ($\geq$513.9 $\pm$ 61.6 mC/cm^2) by 2 orders of magnitude. In order to identify safe stimulation ranges, biphasic, charge-balanced, cathodic-first, symmetric current pulses of increasing amplitude were applied to 25 μm diameter CNT electrodes in PBS. Periodic monitoring of the electrode impedance and equivalent circuit analysis clearly revealed the onset of gas evolution. The maximum stimulation charge density of 40.7 mC/cm^2 translates into electrode diameters as small as 5.3 μm theoretically capable of delivering threshold charges for neural activation. In addition, prolonged stimulation with 5000 biphasic current pulses at 8.1, 40.7, and 81.5 mC/cm^2 increased the CNT electrode impedance at 1 kHz only by 5.5, 1.2, and 12.1%, respectively. This work represents an innovative approach toward realizing advanced CMOS-based neural probes for high-resolution neural recording and stimulation.

MATERIALS AND METHODS

Device Fabrication. Processing was carried out on 200 mm Si wafers with 300 nm thermal oxide on both the front and back sides. Metal interconnects, bond pads, and electrode areas were defined by lift-off of sputter-deposited Ti/Pt/Ti (20 nm/200 nm/ 20 nm) (Nimbus XP, Nexx Systems, USA) using LOR10A (Microchem, USA) as the under-layer and IX845 (JSR-Micro, USA) as the photoresist. In a second lift-off step, TiN (100 nm; Nimbus XP, Nexx Systems, USA) was selectively patterned on top of the electrode areas followed by RF sputtering of a thin, 2 nm thick (nominal) Ni layer (A610 sputter system, Alcatel, USA). Multiwalled CNTs were grown in a 200 mm microwave (2.45 GHz) PECVD chamber (TEL, Japan). The microwave plasma source was located remotely from the wafer surface to avoid excessive

ion-bombardment favoring CNT formation over fiber-like structures. The CNT growth temperature was fixed at 425 °C to be compatible with Cu-BEOL CMOS processing. Furthermore, at this temperature, Ni is an effective catalyst for CNT growth because it is reduced to its catalytically active metallic state. In a typical CNT growth experiment, this Ni film was transformed into active metal nanoparticles in a NH_3 plasma for 5 min. The CNTs were then grown in a gas atmosphere of C_2H_4/H_2 at 3 Torr for 30 min, resulting in a CNT density of 2×10^{11} cm^{-2}, a height of 2 μm, and an average nanotube diameter of 34 nm. A 300 nm thick SiO_2 layer deposited by CVD at 150 °C (Plasmalab 80, Oxford Instruments, UK) served as the protection of the CNTs. As an effective and biocompatible insulation material, we evaporated 1 μm of Parylene C (PDS 2010 Labcoater 2, SCS, USA). The bond pads were opened by RIE (SPTS, UK) of the Parylene C (130 s; 30 sccm SF_6, 200 sccm O_2, 100 Torr, 250 W) and SiO_2 (90 s; 10 sccm O_2, 100 sccm SF_6, 100 Torr, 200 W) using a resist etch mask (IX845, JSR-Micro, USA). In a second RIE step, the Parylene C on top of the contact areas was etched. An etch time of 130 s was sufficient to remove the Parylene C and leave the SiO_2 coating intact. After wafer dicing, the singulated chips were wire-bonded onto custom PCBs and sealed with epoxy (353ND-T, Epotek, USA). Prior to electrochemical experimentation, the SiO_2 layer on top of the CNT electrodes was removed by dipping the packaged chips in BHF for 1.5 min. Inspection was performed by SEM (SU8000, Hitachi, Japan) and combined FIB/SEM analysis (Nova 600 Dual-Beam, FEI, USA).

Electrochemical Characterization. Electrochemical measurements were performed in PBS (0.150 M NaCl, 0.016 M Na_2HPO_4, 0.004 M KH_2PO_4, pH 7.4). All chemicals were analytical grade and used as delivered (Sigma-Aldrich, USA). Experiments were conducted in a glass beaker using a three-electrode configuration placed inside a Faraday cage. A commercial double-junction Ag|AgCl (3 M KCl) reference electrode (Radiometer Analytical, France) was used together with a large-area Pt counter electrode. Measurements were made using an Autolab PSTAT302N potentiostat with integrated frequency response analyzer controlled by the NOVA software (version 1.6, Ecochemie, Netherlands). An additional low-current amplifier module (ECD, Ecochemie, Netherlands) was used for low-current CV measurements with the 5 μm diameter electrodes. Stimulation experiments required an additional AD converter (ADC10M, Ecochemie, The Netherlands) for high-speed sampling at 250 kHz. All impedance measurements were performed after establishment of the open-circuit potential, that is, after the electrode potential change dropped below 100 μV/s. We used OriginPro 8.5 (Originlab, USA) and ZView (Scribner, USA) for the data analysis and the nonlinear least-squares fitting of the EIS spectra, respectively. The experimental sequence for all electrodes consisted of an initial electrochemical cleaning step where the electrode potential was cycled at 2 V/s between the respective limits of gas evolution until a stable and reproducible response was observed, followed by 10 slow-sweep CV cycles at 0.1 V/s and the EIS with a 10 mV (rms) AC signal applied between 1 and 10^5 Hz. The CSC_c was obtained from the 10th slow-sweep CV cycle.

Analysis by FTIR. We performed FTIR analysis on as-grown CNTs synthesized as described above on wafers uniformly coated with TiN/Ni (100 nm/2 nm), on CNTs immersed in BHF for 1.5 min, and on CNTs coated with CVD SiO_2 (300 nm) and immersed in BHF for 1.5 min. All spectra were collected in transmittance (%) mode (IFS 66 v/S, Bruker Optics, Germany) over the wavenumber range of 500–4000 cm^{-1}. Recorded spectra were corrected for baseline and analyzed using OriginPro 8.5 (Originlab, USA).

Brain Extraction and Insertion. Female Wistar rats were euthanized by CO_2 inhalation. After decapitation, the brain was extracted and immersed in ice-cold PBS. Implantations were performed immediately after extraction. The chips were fastened to a microdrive in order to allow for controlled insertion. After removal from the brain, the chips were briefly rinsed in DI water and lightly dried with N_2.

REFERENCES AND NOTES

1. Csicsvari, J.; Henze, D. A.; Jamieson, B.; Harris, K. D.; Sirota, A.; Bartho, P.; Wise, K. D.; Buzsaki, G. Massively Parallel Recording of Unit and Local Field Potentials with Silicon-Based Electrodes. *J. Neurophysiol.* **2003**, *90*, 1314–1323.

2. Hochberg, L. R.; Serruya, M. D.; Friehs, G. M.; Mukand, J. A.; Saleh, M.; Caplan, A. H.; Branner, A.; Chen, D.; Penn, R. D.; Donoghue, J. P. Neuronal Ensemble Control of Prosthetic Devices by a Human with Tetraplegia. *Nature* **2006**, *442*, 164–171.

3. Perlmutter, J. S.; Mink, J. W. Deep Brain Stimulation. *Annu. Rev. Neurosci.* **2006**, *29*, 229–257.

4. Cogan, S. F. Neural Stimulation and Recording Electrodes. *Annu. Rev. Biomed. Eng.* **2008**, *10*, 275–309.

5. Whalen, J. J.; Young, J.; Weiland, J. D.; Searson, P. C. Electrochemical Characterization of Charge Injection at Electrodeposited Platinum Electrodes in Phosphate Buffered Saline. *J. Electrochem. Soc.* **2006**, *153*, C834–C839.

6. Negi, S.; Bhandari, R.; Rieth, L.; Wagenen, R. V.; Solzbacher, F. Neural Electrode Degradation from Continuous Electrical Stimulation: Comparison of Sputtered and Activated Iridium Oxide. *J. Neurosci. Methods* **2010**, *186*, 8–17.

7. Wilks, S. J.; Richardson-Burns, S. M.; Hendricks, J. L.; Martin, D. C.; Otto, K. J. Poly(3,4-ethylene dioxythiophene) (PEDOT) as a Micro-Neural Interface Material for Electrostimulation. *Front. Neuroeng.* **2009**, *2*, 1–88.

8. Gabay, T.; Ben-David, M.; Kalifa, I.; Sorkin, R.; Abrams, Z. R.; Ben-Jacob, E.; Hanein, Y. Electro-chemical and Biological Properties of Carbon Nanotube Based Multi-electrode Arrays. *Nanotechnology* **2007**, *18*, 1–6.

9. Keefer, E. W.; Botterman, B. R.; Romero, M. I.; Rossi, A. F.; Gross, G. W. Carbon Nanotube Coating Improves Neuronal Recordings. *Nat. Nanotechnol.* **2008**, *3*, 434–439.

10. Jan, E.; Hendricks, J. L.; Husaini, V.; Richardson-Burns, S. M.; Sereno, A.; Martin, D. C.; Kotov, N. A. Layered Carbon Nanotube-Polyelectrolyte Electrodes Outperform Traditional Neural Interface Materials. *Nano Lett.* **2009**, *9*, 4012–4018.

11. Cogan, S. F.; Guzelian, A. A.; Agnew, W. F.; Yuen, T. G. H.; McCreery, D. B. Over-Pulsing Degrades Activated Iridium Oxide Films Used for Intracortical Neural Stimulation. *J. Neurosci. Methods* **2004**, *137*, 141–150.

12. Green, R. A.; Williams, C. M.; Lovell, N. H.; Poole-Warren, L. A. Novel Neural Interface for Implant Electrodes: Improving Electroactivity of Polypyrrole through MWNT Incorporation. *J. Mater. Sci. Mater. Med.* **2008**, *19*, 1625–1629.

13. Lee, S. W.; Yabuuchi, N.; Gallant, B. M.; Chen, S.; Kim, B.-S.; Hammond, P. T.; Shao-Horn, Y. High-Power Lithium Batteries from Functionalized Carbon-Nanotube Electrodes. *Nat. Nanotechnol.* **2010**, *5*, 531–537.

14. Mattson, M. P.; Haddon, R. C.; Rao, A. M. Molecular Functionalization of Carbon Nanotubes and Use as Substrates for Neuronal Growth. *J. Mol. Neurosci.* **2000**, *14*, 175–182.

15. Lovat, V.; Pantarotto, D.; Lagostena, L.; Cacciari, B.; Grandolfo, M.; Righi, M.; Spalluto, G.; Prato, M.; Ballerini, L. Carbon Nanotube Substrates Boost Neuronal Electrical Signaling. *Nano Lett.* **2005**, *5*, 1107–1110.

16. Liopo, A. V.; Stewart, M. P.; Hudson, J.; Tour, J. M.; Pappas, T. C. Biocompatibility of Native and Functionalized Single-Walled Carbon Nanotubes for Neuronal Interface. *J. Nanosci. Nanotechnol.* **2006**, *6*, 1365–1374.

17. Smart, S. K.; Cassady, A. I.; Lu, G. Q.; Martin, D. J. The Biocompatibility of Carbon Nanotubes. *Carbon* **2006**, *44*, 1034–1047.

18. Mazzatenta, A.; Giugliano, M.; Campidelli, S.; Gambazzi, L.; Businaro, L.; Markram, H.; Prato, M.; Ballerini, L. Interfacing Neurons with Carbon Nanotubes: Electrical Signal Transfer

and Synaptic Stimulation in Cultured Brain Circuits. *J. Neurosci.* **2007**, *27*, 6931–6936.

19. Wang, K.; Fishman, H. A.; Dai, H. J.; Harris, J. S. Neural Stimulation with a Carbon Nanotube Microelectrode Array. *Nano Lett.* **2006**, *6*, 2043–2048.

20. Liu, X.; Baronian, K. H. R.; Downard, A. J. Patterned Arrays of Vertically Aligned Carbon Nanotube Microelectrodes on Carbon Films Prepared by Thermal Chemical Vapor Deposition. *Anal. Chem.* **2008**, *80*, 8835–8839.

21. Chen, C.-H.; Su, H.-C.; Chuang, S.-C.; Yen, S.-J.; Chen, Y.-C.; Lee, Y.-T.; Chen, H.; Yew, T.-R.; Chang, Y.-C.; Yeh, S.-R.; Yao, D.-J. Hydrophilic Modification of Neural Microelectrode Arrays Based on Multi-walled Carbon Nanotubes. *Nanotechnology* **2010**, *21*, 485501–485510.

22. Shoval, A.; Adams, C.; David-Pur, M.; Shein, M.; Hanein, Y.; Sernagor, E. Carbon Nanotube Electrodes for Effective Interfacing with Retinal Tissue. *Front. Neuroeng.* **2010**, *3*, 1–8.

23. Fung, A. O.; Tsiokos, C.; Paydar, O.; Chen, L. H.; Jin, S.; Wang, Y.; Judy, J. W. Electrochemical Properties and Myocyte Interaction of Carbon Nanotube Microelectrodes. *Nano Lett.* **2010**, *10*, 4321–4327.

24. Hsu, H.-L.; Teng, I.-J.; Chen, Y.-C.; Hsu, W.-L.; Lee, Y.-T.; Yen, S.-J.; Su, H.-C.; Yeh, S.-R.; Chen, H.; Yew, T.-R. Flexible UV-Ozone-Modified Carbon Nanotube Electrodes for Neuronal Recording. *Adv. Mater.* **2010**, *22*, 2177–2181.

25. Gabriel, G.; Gómez, R.; Bongard, M.; Benito, N.; Fernández, E.; Villa, R. Easily Made Single-Walled Carbon Nanotube Surface Microelectrodes for Neuronal Applications. *Biosens. Bioelectron.* **2009**, *24*, 1942–1948.

26. Lin, C.-M.; Lee, Y.-T.; Yeh, S.-R.; Fang, W. Flexible Carbon Nanotubes Electrode for Neural Recording. *Biosens. Bioelectron.* **2009**, *24*, 2791–2797.

27. Fuchsberger, K.; Goff, A. L.; Gambazzi, L.; Toma, F. M.; Goldoni, A.; Giugliano, M.; Stelzle, M.; Prato, M. Multiwalled Carbon-Nanotube-Functionalized Microelectrode Arrays Fabricated by Microcontact Printing: Platform for Studying Chemical and Electrical Neuronal Signaling. *Small* **2011**, *7*, 524–530.

28. Cott, D.; Chiodarelli, N.; Vereecken, P. M.; Vereecke, B.; Van Elshocht, S.; De Gendt, S. A CMOS Compatible Carbon Nanotube Growth Approach. *Proc. 2010 MRS Fall Meeting* **2011**, C4.11.

29. Chen, Y.-C. An Active, Flexible Carbon Nanotube Microelectrode Array for Recording Electrocorticograms. *J. Neural Eng.* **2011**, *8*, 034001.

30. Kotov, N.; Winter, J.; Clements, I.; Jan, E.; Timko, B.; Campidelli, S. Nanomaterials for Neural Interfaces. *Adv. Mater.* **2009**, *21*, 3970–4004.

31. Ansaldo, A.; Castagnola, E.; Maggiolini, E.; Fadiga, L.; Ricci, D. Superior Electrochemical Performance of Carbon Nanotubes Directly Grown on Sharp Microelectrodes. *ACS Nano* **2011**, *5*, 2206–2214.

32. Shein, M.; Greenbaum, A.; Gabay, T.; Sorkin, R.; David-Pur, M.; Ben-Jacob, E.; Hanein, Y. Engineered Neuronal Circuits Shaped and Interfaced with Carbon Nanotube Microelectrode Arrays. *Biomed. Microdevices* **2009**, *11*, 495–501.

33. Li, J.; Ng, H. T.; Cassell, A.; Fan, W.; Chen, H.; Ye, Q.; Koehne, J.; Han, J.; Meyyappan, M. Carbon Nanotube Nanoelectrode Array for Ultrasensitive DNA Detection. *Nano Lett.* **2003**, *3*, 597–602.

34. Chiodarelli, N.; Li, Y.; Cott, D. J.; Mertens, S.; Peys, N.; Heyns, M.; De Gendt, S.; Groeseneken, G.; Vereecken, P. M. Integration and Electrical Characterization of Carbon Nanotube via Interconnects. *Microelectron. Eng.* **2011**, *88*, 837–843.

35. Pan, B.; Xing, B. S. Adsorption Mechanisms of Organic Chemicals on Carbon Nanotubes. *Environ. Sci. Technol.* **2008**, *42*, 9005–9013.

36. Lin, Y.; Watson, K. A.; Fallbach, M. J.; Ghose, S.; Smith, J. G.; Delozier, D. M.; Cao, W.; Crooks, R. E.; Connell, J. W. Rapid, Solventless, Bulk Preparation of Metal Nanoparticle-Decorated Carbon Nanotubes. *ACS Nano* **2009**, *3*, 871–884.

37. Schmitt, G.; Schultze, J.-W.; Fassbender, F.; Buss, G.; Lüth, H.; Schöning, M. Passivation and Corrosion of Microelectrode Arrays. *Electrochim. Acta* **1999**, *44*, 3865–3883.

38. Li, W.; Rodger, D. C.; Meng, E.; Weiland, J. D.; Humayun, M. S.; Tai, Y.-C. Wafer-Level Parylene Packaging with Integrated RF Electronics for Wireless Retinal Prostheses. *J. Microelectromech. Syst.* **2010**, *19*, 735–742.

39. Black, R.; Hannaker, P. Dissolution of Smooth Platinum Electrodes in Biological Fluids. *Appl. Neurophysiol.* **1979**, *42*, 366–374.

40. Robblee, L.; McHardy, J.; Agnew, W.; Bullara, L. Electrical Stimulation with Pt Electrodes. VII. Dissolution of Pt Electrodes during Electrical Stimulation of the Cat Cerebral Cortex. *J. Neurosci. Methods* **1983**, *9*, 301–308.

41. Morton, S. L.; Daroux, M. L.; Mortimer, J. T. The Role of Oxygen Reduction in Electrical Stimulation of Neural Tissue. *J. Electrochem. Soc.* **1994**, *141*, 122–130.

42. Huang, C. Q.; Carter, P. M.; Shepherd, R. K. Stimulus Induced pH Changes in Cochlear Implants: An *In Vitro* and *In Vivo* Study. *Annu. Rev. Biomed. Eng.* **2001**, *29*, 791–802.

43. Cogan, S.; Ehrlich, J.; Plante, T.; Gingerich, M.; Shire, D. Contribution of Oxygen Reduction to Charge Injection on Platinum and Sputtered Iridium Oxide Neural Stimulation Electrodes. *IEEE Trans. Biomed. Eng.* **2010**, *57*, 2313–2321.

44. Robblee, L. S.; Rose, T. L. In *Neural Prostheses: Fundamental Studies*; Agnew, W. F., McCreery, D. B., Eds.; Prentice Hall: Englewood Cliffs, NJ, 1990.

45. Scholz, F., Ed. *Electroanalytical Methods*; Springer: Heidelberg, 2010; Chapter II.1, pp 57−106.

46. Musa, S.; Rand, D. R.; Bartic, C.; Eberle, W.; Nuttin, B.; Borghs, G. Coulometric Detection of Irreversible Electrochemical Reactions Occurring at Pt Microelectrodes Used for Neural Stimulation. *Anal. Chem.* **2011**, *83*, 4012–4022.

47. Azumi, K.; Watanabe, S.; Seo, M.; Saeki, I.; Inokuchi, Y.; James, P.; Smyrl, W. H. Characterization of Anodic Oxide Film Formed on TiNx Coating in Neutral Borate Buffer Solution. *Corros. Sci.* **1998**, *40*, 1363–1377.

48. Milosev, I.; Strehblow, H. H.; Navinsek, B.; Metikos-Hukovic, M. Electrochemical and Thermal Oxidation of TiN Coatings Studied by XPS. *Surf. Interface Anal.* **1995**, *23*, 529–39.

49. Avasarala, B.; Haldar, P. Electrochemical Oxidation Behavior of Titanium Nitride Based Electrocatalysts Under PEM Fuel Cell Conditions. *Electrochim. Acta* **2010**, *55*, 9024–9034.

50. Barisci, J. N.; Wallace, G. G.; Baughman, R. H. Electrochemical Characterization of Single-Walled Carbon Nanotube Electrodes. *J. Electrochem. Soc.* **2000**, *147*, 4580–4583.

51. Bard, A. J.; Faulkner, L. R. *Electrochemical Methods: Fundamentals and Applications*, 2nd ed.; John Wiley Sons: New York, 2001.

52. Lasia, A. In *Modern Aspects of Electrochemistry*; Schlesinger, M., Ed.; Springer: Berlin, 2009; Vol. 43; Chapter 3.

53. Moffitt, M. A.; McIntyre, C. C. Model-Based Analysis of Cortical Recording with Silicon Microelectrodes. *Clin. Neurophysiol.* **2005**, *116*, 2240–2250.

54. Lempka, S. F.; Johnson, M. D.; Moffitt, M. A.; Otto, K. J.; Kipke, D. R.; McIntyre, C. C. Theoretical Analysis of Intracortical Microelectrode Recordings. *J. Neural Eng.* **2011**, *8*, 045006.

55. Ferguson, J. E.; Boldt, C.; Redish, A. D. Creating Low-Impedance Tetrodes by Electroplating with Additives. *Sens. Actuators, A* **2009**, *156*, 388–393.

56. Baranauskas, G.; Maggiolini, E.; Castagnola, E.; Ansaldo, A.; Mazzoni, A.; Angotzi, G. N.; Vato, A.; Ricci, D.; Panzeri, S.; Fadiga, L. Carbon Nanotube Composite Coating of Neural Microelectrodes Preferentially Improves the Multiunit Signal-to-Noise Ratio. *J. Neural Eng.* **2011**, *8*, 066013.

57. Butt, H.; Graf, K.; Kappl, M. *Physics and Chemistry of Interfaces*; Wiley-VCH: Weinheim, Germany, 2003.

58. Conway, B. E. *Electrochemical Supercapacitors: Scientific Fundamentals and Technological Applications*; Kluwer Academic/Plenum: New York, 1999.

59. West, A.; Newman, J. Current Distribution on Recessed Electrodes. *J. Electrochem. Soc.* **1991**, *138*, 1620–1625.

60. Conway, B. E.; Pell, W. G. Power Limitations of Supercapacitor Operation Associated with Resistance and Capacitance Distribution in Porous Electrode Devices. *J. Power Sources* **2002**, *105*, 169–81.

ARTICLE

61. Gubellini, P.; Salin, P.; Kerkerian-Le Goff, L.; Baunez, C. Deep Brain Stimulation in Neurological Diseases and Experimental Models: From Molecule to Complex Behavior. *Progr. Neurobiol.* **2009**, *89*, 79–123.

62. Rousche, P.; Normann, R. Chronic Intracortical Microstimulation (ICMS) of Cat Sensory Cortex Using the Utah Intracortical Electrode Array. *IEEE Trans. Neural Syst. Rehab. Eng.* **1999**, *7*, 56–68.

63. Li, P.; Lim, X.; Zhu, Y.; Yu, T.; Ong, C.-K.; Shen, Z.; Wee, A. T.-S.; Sow, C.-H. Tailoring Wettability Change on Aligned and Patterned Carbon Nanotube Films for Selective Assembly. *J. Phys. Chem. B* **2007**, *111*, 1672–1678.

64. Magrez, A.; Kasas, S.; Salicio, V.; Pasquier, N.; Seo, J. W.; Celio, M.; Catsicas, S.; Schwaller, B.; Forró, L. Cellular Toxicity of Carbon-Based Nanomaterials. *Nano Lett.* **2006**, *6*, 1121–1125.

65. Moon, J. S.; Alegaonkar, P. S.; Han, J. H.; Lee, T. Y.; Yoo, J. B.; Kim, J. M. Enhanced Field Emission Properties of Thin-Multiwalled Carbon Nanotubes: Role of SiOx Coating. *J. Appl. Phys.* **2006**, *100*, 1043031–7.

66. Kim, U. J.; Liu, X. M.; Furtado, C. A.; Chen, G.; Saito, R.; Jiang, J.; Dresselhaus, M. S.; Eklund, P. C. Infrared-Active Vibrational Modes of Single-Walled Carbon Nanotubes. *Phys. Rev. Lett.* **2005**, *95*, 157402–4.

67. Socrates, G. *Infrared and Raman Characteristic Group Frequencies*; Wiley & Sons: New York, 2001.

68. Kim, U. J.; Furtado, C. A.; Liu, X.; Chen, G.; Eklund, P. C. Raman and IR Spectroscopy of Chemically Processed Single-Walled Carbon Nanotubes. *J. Am. Chem. Soc.* **2005**, *127*, 15437–15445.

69. Liu, M.; Yang, Y.; Zhu, T.; Liu, Z. Chemical Modification of Single-Walled Carbon Nanotubes with Peroxytrifluoroacetic Acid. *Carbon* **2005**, *43*, 1470–1478.

70. Liu, H.; Li, S. H.; Zhai, J.; Li, H. J.; Zheng, Q. S.; Jiang, L.; Zhu, D. B. Self-Assembly of Large-Scale Micropatterns on Aligned Carbon Nanotube Films. *Angew. Chem., Int. Ed.* **2004**, *43*, 1146–1149.